IEEE Access
Multidisciplinary | Rapid Review | Open Access Journal

Received May 14, 2018, accepted June 25, 2018, date of publication June 29, 2018, date of current version September 21, 2018.

Digital Object Identifier 10.1109/ACCESS.2018.2851454

A Theoretical Model for Designing the Novel Embeddable Spherical Smart Aggregate

JIANJUN WANG[1], QINGZHAO KONG[2], (Member, IEEE), ZHIFEI SHI[3], AND GANGBING SONG[2], (Member, IEEE)

[1]Department of Applied Mechanics, University of Science and Technology Beijing, Beijing 100083, China
[2] Department of Mechanical Engineering, University of Houston, Houston, TX 77204, USA
[3]School of Civil Engineering, Beijing Jiaotong University, Beijing 100044, China

Corresponding author: Gangbing Song (gsong@uh.edu)

This work was supported in part by the National Natural Science Foundation of China under Grant 51472022 and Grant 51708025 and in part by the Fundamental Research Funds for the Central Universities under Grant FRF-TP-16-069A1.

ABSTRACT A type of novel embeddable spherical smart aggregate (SSA) has been developed successfully in the latest work. The SSA is formed by encapsulating a radially polarized spherical piezoceramic shell with epoxy resin and a spherical ultra-high performance concrete (UHPC) case, and its omnidirectional actuating and sensing capabilities in concrete structures have also been verified. Comparing to the early developed compressive and shear mode smart aggregates (SAs) that can only generate or receive the stress wave in a single direction, the SSA can generate or receive omnidirectional stress waves, which has a promising application in structural health monitoring of civil engineering structures. To understand better the performance of the SSA and guiding further its optimized design, a theoretical model is proposed to study the vibration characteristics of the SSA in this paper. Based on the linear theory of piezoelasticity, the dynamic analytical solution of an SSA subjected to a harmonic voltage excitation is derived, and the analytical expression of the electrical impedance is obtained. Furthermore, a parametric analysis is conducted to discuss the effects of the outer radius of the UHPC case, the thickness of the epoxy layer, the inner radius of the piezoceramic shell, the piezoelectric material types, and the piezoelectric material parameters on the vibration characteristics, such as the first and second resonance and anti-resonance frequencies. Furthermore, comparisons with some special cases in the previous work, the ANSYS simulation results and the experimental data of the SSA are also given to validate the reliability of the proposed model. The present investigations contribute to the comprehensive understanding of the vibration characteristics of the SSA, which is helpful to design the working frequencies range of the SSA.

INDEX TERMS Spherical smart aggregate (SSA), spherical piezoceramic shell, vibration characteristics, piezoelasticity.

I. INTRODUCTION

PIEZOCERAMIC material is one of the most important smart materials due to its unique positive and negative piezoelectric effects, which has been extensively used in actuators [1], [2], sensors [3], [4], energy harvesters [5]–[8], transformers [9], [10], transducers [11], [12] for many fields such as mechanical engineering, civil engineering, medical engineering, aeronautical and space engineering. In recent years, structural health monitoring of civil engineering structures is receiving considerable attention and has become a hot research topic. Smart aggregates (SAs) are a type of novel piezoceramic-based multi-functional transducers that are designed based on Lead Zirconate Titanate (PZT), which have promising application in structural health monitoring of civil engineering structures [13], [14]. In the past decade, two generations of SAs have been successively developed. The first generation of SA was formed by embedding a thin waterproof PZT patch with lead wires into a casted concrete block [15]. The SA not only has advantages such as low cost, fast response, embeddability, good compatibility with concrete structures and simple implementation [16], [17], but also has outstanding actuating and sensing capabilities that can serve as an actuator or a sensor to generate or receive the stress wave signals [15], [18]. Since then, the SA based structural health monitoring in civil engineering has attracted more and more attention. Many researches have been obtained,

including concrete early-age strength monitoring [15], collapse detection [16], crack detection [18]–[20], health status evaluation [21], active interface debonding detection [22], impact loading measurement [23], monitoring of the ultrasonic P-wave velocity in early-age concrete [24], reinforced concrete structural impact damage detection [25]. Another successful application of the SA is to monitor traffic flow in public transportation [26], [27]. In addition, a kind of design called 2-2 cement based piezoelectric composite was also fabricated by Li *et al*. [28] and Zhang *et al*. [29] and Xu *et al*. [30], [31], respectively. This design extends the single PZT patch to the multiple PZT patches, which can effectively improve the electromechanical performance of the SA.

The second generation of SA was fabricated by sandwiching PZT patches between two marble pieces with epoxy, which is proposed by Hou *et al*. [32], [33] and Kong *et al*. [34], [35]. The aim of this new design is to improve the survivability of the SAs when the concrete structures are overloaded. In addition to processing the performance of the first generation of SA, the second generation of SAs have a unique advantage that can survive in the crushing stage of concrete structures [32], [33]. Applications of the second generation of SAs also involved soil freeze-thaw process monitoring [35], very early age concrete hydration monitoring [36], water seepage monitoring [17], [37], impact location estimation [38], concrete seismic stress monitoring [32], [33], [39], bond slip detection [40], damage detection [41], flexural cracks detection and monitoring [42] and water presence detection [43], assessment of the porosity in cementitious materials [44], stress monitoring of sand-filled steel tube during impact [45], real-time evaluation of concrete surface crack repairing [46], detection of debonding between fiber reinforced polymer bar and concrete structure [47], monitoring of corrosion-induced degradation in prestressed concrete structure [48], real-time monitoring of water content in sandy soil [49]. In addition, the performance of this type of SAs under complex conditions, such as various compressive stresses [50], water environment [51], various environmental temperatures [52] and axial loads [53], were also demonstrated clearly.

These studies mentioned above have greatly promoted the development of the SA based structural health monitoring in civil engineering. However, there are still some limitations about the directivity of the stress waves. Due to the geometry of the two-dimensional PZT patch, the SAs usually utilize compressive mode (d_{33} mode) or shear mode (d_{15} mode) to generate or receive the stress waves in a single direction. But in many cases, for example when the locations of the damages or impacts are unpredictable, numbers of the SAs must be deployed to achieve an adequate detection aperture, which will cause complications in SA installation, wire management and data acquisition, and finally lead to additional economic and labor burden. A type of radially polarized spherical piezoceramic shells have exhibited the unique omnidirectional sound transmitting and receiving capabilities in the applications of underwater acoustic detection, ultrasonic imaging, hydrophones and nondestructive testing [54]–[61], which provides a good candidate for developing the improved SA in civil engineering. In the latest work, a type of novel embeddable spherical smart aggregate (SSA) was developed successfully based on the radially polarized spherical piezoceramic shell [62], and its omnidirectional actuating and sensing capabilities in a one cubic foot concrete specimen were also verified [63]. The proposed SSA has a promising application in structural health monitoring of civil engineering structures. To better understand the vibration characteristics of the SSA and guide further its optimal design, a reasonable theoretical model is very valuable and helpful. Piezo-elasticity theory has been successfully used to solve the dynamic problem of various piezoelectric structures, such as marble-based SA [64], 2-2 cement based piezoelectric transducers [65], [66], multilayer piezoelectric composite cylindrical transducers [67], [68], circular cylindrical piezoelectric transformers [69], [70], piezoceramic/metal sandwich cylindrical transducers [71]–[73], spherical piezoelectric transducers [55], [74], functionally graded piezoelectric spherical shells [75].

The aim of this paper is to propose a simplified theoretical model based on the linear theory of piezo-elasticity to investigate the vibration characteristics of the spherical smart aggregates in the hope of understanding comprehensively the vibration characteristics of the SSA and guiding further its optimized design. The rest of the paper is organized as follow: Section II first introduces the schematic of the SSA, and then summarizes its basic equations. Section III first solves the dynamic analytical solution of the SSA subjected to a harmonic voltage excitation, and then derives the analytical expression of the electric impedance. Section IV presents a parametric analysis to discuss the effects of the outer radius of the UHPC case, the thickness of the epoxy layer, the inner radius of the piezoceramic shell, the piezoelectric material types and the piezoelectric material parameters on the vibration characteristics. Section V performs comparisons with some special cases in the previous work, the ANSYS simulation results and the experimental data of the SSA to validate the proposed model. Section VI concludes the entire paper.

II. BASIC EQUATIONS

As shown in Fig. 1, a fabricated embeddable spherical smart aggregate (SSA) and its schematic are exhibited. In this novel design, a radially polarized spherical piezoceremic shell is used as the main functional element that can generate and receive omni-directional stress waves. A whole spherical ultra-high performance concrete (UHPC) case formed by two hemi-spherical cases is proposed to protect the fragile spherical piezoceremic shell that can provide the unparalleled survival rate. A wire is threaded from the internal and external electrodes of the spherical piezoceremic shell. All the above these parts are assembled together using epoxy resin. Furthermore, to simplify modeling and analysis, the SSA

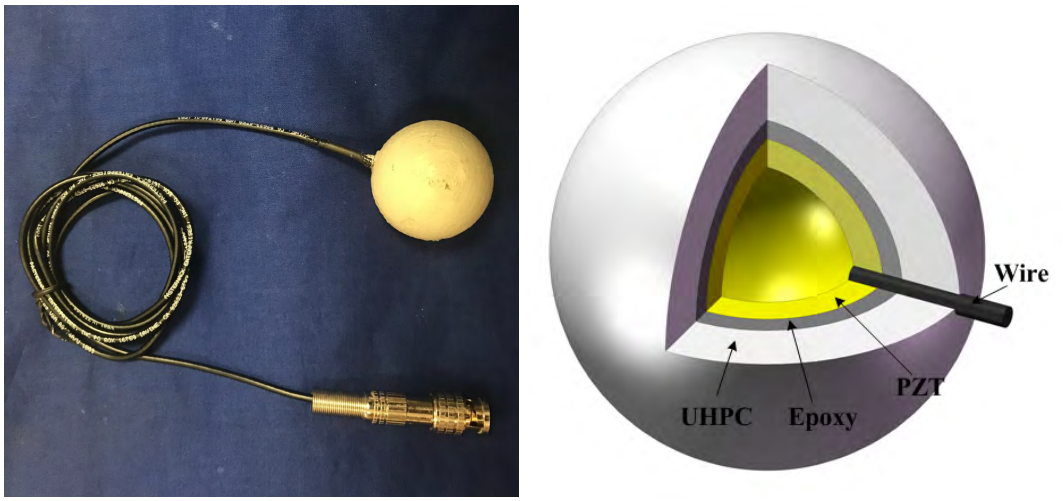

FIGURE 1. The fabricated spherical smart aggregate and its schematic.

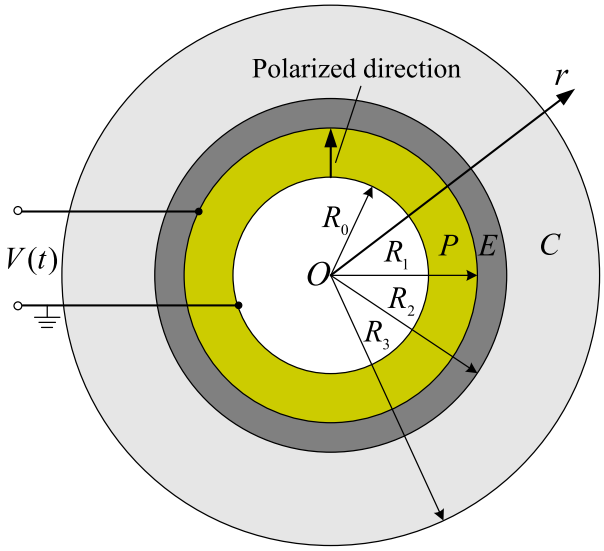

FIGURE 2. A simplified model for spherical smart aggregate.

is considered as the perfect spherical structure, as shown in Fig. 2. PZT, Epoxy and UHPC are denoted as symbols P, E and C, respectively. The thicknesses of PZT layer, Epoxy layer and UHPC layer are determined by $(R_1 - R_0)$, $(R_2 - R_1)$ and $(R_3 - R_2)$, respectively. PZT layer is polarized along its radial direction.

For the PZT layer, $\varepsilon_{\theta P}$ and ε_{rP} denote the circumferential and radial strain components, respectively; $\sigma_{\theta P}$ and σ_{rP} denote the circumferential and radial stress components, respectively; E_r and D_r denote the radial electric field and electric displacement, respectively. The linear constitutive equations about the spherically symmetric problem can be described as [76]–[78]

$$\sigma_{\theta P} = (c_{11}^E + c_{12}^E)\varepsilon_{\theta P} + c_{13}^E \varepsilon_{rP} - e_{31} E_r \tag{1}$$

$$\sigma_{rP} = 2c_{13}^E \varepsilon_{\theta P} + c_{33}^E \varepsilon_{rP} - e_{33} E_r \tag{2}$$

$$D_r = 2e_{31}\varepsilon_{\theta P} + e_{33}\varepsilon_{rP} + \kappa_{33}^{\varepsilon} E_r \tag{3}$$

where c_{11}^E, c_{12}^E, c_{13}^E and c_{33}^E are the elastic constants; e_{31} and e_{33} are the piezoelectric constants; $\kappa_{33}^{\varepsilon}$ is the dielectric constant.

The motion equation of the spherical-symmetric vibration can be expressed as [76]–[78]

$$\frac{\partial \sigma_{rP}}{\partial r} + \frac{2(\sigma_{rP} - \sigma_{\theta P})}{r} = \rho_P \frac{\partial^2 u_{rP}}{\partial t^2} \tag{4}$$

where ρ_P and u_{rP} are the density and the radial displacement of PZT layer, respectively. Furthermore, the geometric relationship equations of the strain-displacement and the electrical field-potential ϕ can be expressed as

$$\varepsilon_{rP} = \frac{\partial u_{rP}}{\partial r}, \quad \varepsilon_{\theta P} = \frac{u_{rP}}{r} \tag{5}$$

$$E_r = -\frac{\partial \phi}{\partial r} \tag{6}$$

In addition, the electrostatic charge equation for spherically symmetric problem is the following

$$\frac{\partial D_r}{\partial r} + \frac{2}{r} D_r = 0 \tag{7}$$

In the present analysis, a harmonic voltage excitation is considered.

$$V(t) = V_0 e^{j\omega t} \tag{8}$$

where V_0 is the amplitude of voltage excitation, $j = \sqrt{-1}$ is the imaginary unit, $\omega = 2\pi f$ is the circular frequency, f is the voltage excitation frequency, t is the time. For the spherical-symmetric steady state vibration, the following expressions can be assumed.

$$(u_{rP}, \phi, E_r, D_r, \sigma_{rP}, \sigma_{\theta P}) = [u_{rP}(r), \phi(r), E_r(r), D_r(r), \sigma_{rP}(r), \sigma_{\theta P}(r)]e^{j\omega t} \tag{9}$$

Solving equation (7) gets

$$D_r(r) = \frac{C_1}{r^2} \tag{10}$$

where C_1 is an undetermined constant to be determined by the boundary conditions.

Substituting equations (5), (6) and (10) into equations (1), (2) and (3) yields

$$\sigma_{\theta P}(r) = a_1\frac{u_{rP}(r)}{r} + a_2\frac{du_{rP}(r)}{dr} + a_3\frac{C_1}{r^2} \tag{11}$$

$$\sigma_{rP}(r) = 2a_2\frac{u_{rP}(r)}{r} + a_4\frac{du_{rP}(r)}{dr} + a_5\frac{C_1}{r^2} \tag{12}$$

$$\phi(r) = \frac{1}{\kappa_{33}^{\varepsilon}}[e_{33}u_{rP}(r) + 2e_{31}\int\frac{u_{rP}(r)}{r}dr + \frac{C_1}{r}] + C_0 \tag{13}$$

where $a_1 = c_{11}^E + c_{12}^E + (2e_{31}^2/\kappa_{33}^{\varepsilon})$, $a_2 = c_{13}^E + (e_{31}e_{33}/\kappa_{33}^{\varepsilon})$, $a_3 = -(e_{31}/\kappa_{33}^{\varepsilon})$, $a_4 = c_{33}^E + (e_{33}^2/\kappa_{33}^{\varepsilon})$, $a_5 = -(e_{33}/\kappa_{33}^{\varepsilon})$. C_0 is an undetermined constant to be determined by the boundary conditions.

Substituting equations (9), (11) and (12) into equation (4) yields

$$\frac{d^2u_{rP}(r)}{dr^2} + \frac{2}{r}\frac{du_{rP}(r)}{dr} + [(k_Pr)^2 - \beta^2]\frac{u_{rP}(r)}{r^2} = \frac{a_6C_1}{r^3} \tag{14}$$

where $k_P = \omega/V_{rP}$, $V_{rP}^2 = a_4/\rho_P$, $\beta^2 = 2(a_1 - a_2)/a_4$, $a_6 = 2a_3/a_4$.

Assuming the $u_{rP}(r)$ is satisfied the following form

$$u_{rP}(r) = r^{-1/2}w_{rP}(r) \tag{15}$$

The equation (14) can be transformed as

$$r^2\frac{d^2w_{rP}(r)}{dr^2} + r\frac{dw_{rP}(r)}{dr} + [(k_Pr)^2 - \nu^2]w_{rP}(r) = a_6C_1r^{-1/2} \tag{16}$$

where $\nu = \sqrt{\beta^2 + 1/4}$.

Solving equation (16) results in [79]

$$w_{rP}(r) = A_PJ_\nu(k_Pr) + B_PY_\nu(k_Pr) + C_1a_6(k_P)^{1/2}s_{-3/2,\nu}(k_Pr) \tag{17}$$

where $J_\nu(k_Pr)$ and $Y_\nu(k_Pr)$ are Bessel functions of the first and second kind, respectively; $s_{u,\nu}(k_Pr)$ is the Lommel function of the first kind. Then, $u_{rP}(r)$ can be expressed as

$$u_{rP}(r) = A_Pr^{-1/2}J_\nu(k_Pr) + B_Pr^{-1/2}Y_\nu(k_Pr) + C_1a_6(k_P)^{1/2}r^{-1/2}s_{-3/2,\nu}(k_Pr) \tag{18}$$

Furthermore, equation (18) can be expressed as

$$u_{rP}(r) = A_Pf_1(r) + B_Pf_2(r) + C_1f_3(r) \tag{19}$$

where $f_1(r)$, $f_2(r)$ and $f_3(r)$ are the functions defined as follows [78].

$$f_1(r) = r^{-1/2}J_\nu(k_Pr) \tag{20}$$

$$f_2(r) = r^{-1/2}Y_\nu(k_Pr) \tag{21}$$

$$f_3(r) = a_6(k_P)^{1/2}r^{-1/2}s_{-3/2,\nu}(k_Pr) \tag{22}$$

Substituting equation (18) into equations (12) and (13) yields

$$\sigma_{rP}(r) = A_Pf_4(r) + B_Pf_5(r) + C_1f_6(r) \tag{23}$$

$$\phi(r) = A_Pf_7(r) + B_Pf_8(r) + C_1f_9(r) + C_0 \tag{24}$$

where $f_4(r)$, $f_5(r)$, $f_6(r)$, $f_7(r)$, $f_8(r)$ and $f_9(r)$ are the functions defined as follows [78].

$$f_4(r) = (2a_2 - a_4/2 - a_4\nu)r^{-3/2}J_\nu(k_Pr) + a_4k_Pr^{-1/2}J_{\nu-1}(k_Pr) \tag{25}$$

$$f_5(r) = (2a_2 - a_4/2 - a_4\nu)r^{-3/2}Y_\nu(k_Pr) + a_4k_Pr^{-1/2}Y_{\nu-1}(k_Pr) \tag{26}$$

$$f_6(r) = a_6(k_P)^{1/2}(2a_2 - a_4/2 - a_4\nu)r^{-3/2}s_{-3/2,\nu}(k_Pr) + a_4a_6(k_P)^{3/2}r^{-1/2}(\nu - 5/2)s_{-5/2,\nu-1}(k_Pr) + a_5r^{-2} \tag{27}$$

$$f_7(r) = \frac{1}{\kappa_{33}^{\varepsilon}}\{e_{33}r^{-1/2}J_\nu(k_Pr) + 2^{1/2}e_{31}(k_P)^{1/2}(k_Pr/2)^{\nu-1/2} \times\frac{1}{(\nu-1/2)\Gamma(\nu+1)}{}_1F_2[\frac{1}{2}(\nu-\frac{1}{2});\frac{1}{2}(\nu-\frac{1}{2})+1, \nu+1;-\frac{(k_Pr)^2}{4}]\} \tag{28}$$

$$f_8(r) = \frac{1}{\kappa_{33}^{\varepsilon}}\{e_{33}r^{-1/2}Y_\nu(k_Pr) + 2^{1/2}(k_P)^{1/2}e_{31}\cot(\nu\pi)(k_Pr/2)^{\nu-1/2} \times\frac{1}{(\nu-1/2)\Gamma(\nu+1)}{}_1F_2[\frac{1}{2}(\nu-\frac{1}{2});\frac{1}{2}(\nu-\frac{1}{2})+1, \nu+1;-\frac{(k_Pr)^2}{4}] + 2^{1/2}(k_P)^{1/2}e_{31}\csc(\nu\pi)(k_Pr/2)^{-\nu-1/2} \times\frac{1}{(-\nu-1/2)\Gamma(1-\nu)} \times{}_1F_2[\frac{1}{2}(-\nu-\frac{1}{2});\frac{1}{2}(-\nu-\frac{1}{2})+1, -\nu+1;-\frac{(k_Pr)^2}{4})]\} \tag{29}$$

$$f_9(r) = \frac{1}{\kappa_{33}^{\varepsilon}}\{e_{33}a_6(k_P)^{1/2}r^{-1/2}s_{-3/2,\nu}(k_Pr) + r^{-1} + 2e_{31}a_6(k_P)^{1/2}\frac{1}{\nu^2 - (1/2)^2} \times[(k_P)^{-1/2}r^{-1} + \frac{1}{(3/2)^2 - \nu^2}(k_P)^{1/2}(k_Pr) \times{}_2F_3(1,\frac{1}{2};\frac{3}{2},\frac{7}{4}+\frac{\nu}{2},\frac{7}{4}-\frac{\nu}{2};-\frac{(k_Pr)^2}{4})]\} \tag{30}$$

In the above equations (28)~(30), $\Gamma(x)$ is the Gamma function. ${}_mF_n(\tilde{\alpha}_1,\cdots,\tilde{\alpha}_m;\tilde{\beta}_1,\cdots,\tilde{\beta}_n;x)$ is the generalized hypergeometric function.

For the Epoxy layer, $\varepsilon_{\theta E}$ and ε_{rE} are adopted to denote the circumferential and radial strain components, respectively; $\sigma_{\theta E}$ and σ_{rE} are used to denote the circumferential and radial stress components, respectively. Thus, the linear constitutive equations for isotropic elastic material can be expressed as [55]

$$\sigma_{\theta E} = 2(\lambda_E + \mu_E)\varepsilon_{\theta E} + \lambda_E\varepsilon_{rE} \tag{31}$$

$$\sigma_{rE} = 2\lambda_E\varepsilon_{\theta E} + (\lambda_E + 2\mu_E)\varepsilon_{rE} \tag{32}$$

where λ_E and μ_E are Lamé constants, and $\lambda_E = E_E v_E / [(1+v_E)(1-2v_E)]$, $\mu_E = E_E / [2(1+v_E)]$. E_E and v_E are Young's modulus and Poisson's ratio of epoxy layer, respectively.

The motion equation of the spherical-symmetric vibration can be expressed as

$$\frac{\partial \sigma_{rE}}{\partial r} + \frac{2(\sigma_{rE} - \sigma_{\theta E})}{r} = \rho_E \frac{\partial^2 u_{rE}}{\partial t^2} \tag{33}$$

where ρ_E and u_{rE} are the density and the radial displacement of epoxy layer, respectively. Furthermore, the geometric relationship equations of the strain-displacement can be expressed as

$$\varepsilon_{rE} = \frac{\partial u_{rE}}{\partial r}, \varepsilon_{\theta E} = \frac{u_{rE}}{r} \tag{34}$$

Considering the spherical-symmetric steady state vibration, u_{rE}, $\sigma_{\theta E}$ and σ_{rE} can be assumed as

$$(u_{rE}, \sigma_{rE}, \sigma_{\theta E}) = [u_{rE}(r), \sigma_{rE}(r), \sigma_{\theta E}(r)]e^{j\omega t} \tag{35}$$

Substituting equations (31), (32), (34) and (35) into equation (33) yields

$$\frac{d^2 u_{rE}(r)}{dr^2} + \frac{2}{r}\frac{du_{rE}(r)}{dr} + [(k_E r)^2 - 2]\frac{u_{rE}(r)}{r^2} = 0 \tag{36}$$

where $k_E = \omega / V_{rE}$, $V_{rE}^2 = (\lambda_E + 2\mu_E)/\rho_E$.

Solving equation (36) results in [55]

$$u_{rE}(r) = A_E r^{-1/2} J_{3/2}(k_E r) + B_E r^{-1/2} Y_{3/2}(k_E r) \tag{37}$$

Furthermore, equation (37) can be expressed as

$$u_{rE}(r) = A_E f_{10}(r) + B_E f_{11}(r) \tag{38}$$

where $f_{10}(r)$ and $f_{11}(r)$ are the functions defined as follows.

$$f_{10}(r) = r^{-1/2} J_{3/2}(k_E r) \tag{39}$$

$$f_{11}(r) = r^{-1/2} Y_{3/2}(k_E r) \tag{40}$$

Substituting equations (34), (35) and (37) into equation (32) yields

$$\sigma_{rE}(r) = A_E f_{12}(r) + B_E f_{13}(r) \tag{41}$$

where $f_{12}(r)$ and $f_{13}(r)$ are the functions defined as follows.

$$\begin{aligned} f_{12}(r) = & -4\mu_E r^{-3/2} J_{3/2}(k_E r) \\ & + (\lambda_E + 2\mu_E) k_E r^{-1/2} J_{1/2}(k_E r) \end{aligned} \tag{42}$$

$$\begin{aligned} f_{13}(r) = & -4\mu_E r^{-3/2} Y_{3/2}(k_E r) \\ & + (\lambda_E + 2\mu_E) k_E r^{-1/2} Y_{1/2}(k_E r) \end{aligned} \tag{43}$$

For the UHPC layer, u_{rC}, $\sigma_{\theta C}$ and σ_{rC} of the spherical-symmetric steady state vibration can be expressed as

$$(u_{rC}, \sigma_{rC}, \sigma_{\theta C}) = [u_{rC}(r), \sigma_{rC}(r), \sigma_{\theta C}(r)]e^{j\omega t} \tag{44}$$

where u_{rC} denotes the radial displacement; σ_{rC} and $\sigma_{\theta C}$ denote circumferential and radial stress components, respectively.

Similarly to solution of the epoxy layer, $u_{rC}(r)$ and $\sigma_{rC}(r)$ in the UHPC layer can be derived as

$$u_{rC}(r) = A_C f_{14}(r) + B_C f_{15}(r) \tag{45}$$

$$\sigma_{rC}(r) = A_C f_{16}(r) + B_C f_{17}(r) \tag{46}$$

where $f_{14}(r), f_{15}(r), f_{16}(r)$ and $f_{17}(r)$ are the functions defined as follows.

$$f_{14}(r) = r^{-1/2} J_{3/2}(k_C r) \tag{47}$$

$$f_{15}(r) = r^{-1/2} Y_{3/2}(k_C r) \tag{48}$$

$$\begin{aligned} f_{16}(r) = & -4\mu_C r^{-3/2} J_{3/2}(k_C r) \\ & + (\lambda_C + 2\mu_C) k_C r^{-1/2} J_{1/2}(k_C r) \end{aligned} \tag{49}$$

$$\begin{aligned} f_{17}(r) = & -4\mu_C r^{-3/2} Y_{3/2}(k_C r) \\ & + (\lambda_C + 2\mu_C) k_C r^{-1/2} Y_{1/2}(k_C r) \end{aligned} \tag{50}$$

In the equations (47) $\sim$ (50), $k_C = \omega / V_{rC}$, $V_{rC}^2 = (\lambda_C + 2\mu_C)/\rho_C$, $\lambda_C = E_C v_C / [(1+v_C)(1-2v_C)]$, $\mu_C = E_C / [2(1+v_C)]$. Here, λ_C and μ_C are Lamé constants of the UHPC material; E_C, ρ_C and v_C are Young's modulus, density and Poisson's ratio of the UHPC material, respectively.

III. SOLUTION

A free-free case is considered in this paper, as shown in Fig. 2. There are two mechanical boundary conditions, two electrical boundary conditions and four continuous conditions at the interfaces. Combining these conditions and the basic equations derived in the previous section, the solution of the SSA can be obtained. The mechanical and electrical boundary conditions as well as continuous conditions can be written as follows, respectively.

$$\begin{cases} \sigma_{rP}|_{r=R_0} = 0 \\ \sigma_{rC}|_{r=R_3} = 0 \end{cases} \tag{51}$$

$$\begin{cases} \phi|_{r=R_0} = 0 \\ \phi|_{r=R_1} = V(t) \end{cases} \tag{52}$$

$$\begin{cases} u_{rP}|_{r=R_1} = u_{rE}|_{r=R_1} \\ \sigma_{rP}|_{r=R_1} = \sigma_{rE}|_{r=R_1} \\ u_{rE}|_{r=R_2} = u_{rC}|_{r=R_2} \\ \sigma_{rE}|_{r=R_2} = \sigma_{rC}|_{r=R_2} \end{cases} \tag{53}$$

Substituting equations (9), (19), (23), (24), (35), (38), (41) and (44)$\sim$(46) into equations (51), (52) and (53), the following equations are obtained.

$$\begin{cases} A_P f_4(R_0) + B_P f_5(R_0) + C_1 f_6(R_0) = 0 \\ A_C f_{16}(R_3) + B_C f_{17}(R_3) = 0 \end{cases} \tag{54}$$

$$\begin{cases} A_P f_7(R_0) + B_P f_8(R_0) + C_1 f_9(R_0) + C_0 = 0 \\ A_P f_7(R_1) + B_P f_8(R_1) + C_1 f_9(R_1) + C_0 = V_0 \end{cases} \tag{55}$$

$$\begin{cases} A_P f_1(R_1) + B_P f_2(R_1) + C_1 f_3(R_1) = A_E f_{10}(R_1) + B_E f_{11}(R_1) \\ A_P f_4(R_1) + B_P f_5(R_1) + C_1 f_6(R_1) = A_E f_{12}(R_1) + B_E f_{13}(R_1) \\ A_E f_{10}(R_2) + B_E f_{11}(R_2) = A_C f_{14}(R_2) + B_C f_{15}(R_2) \\ A_E f_{12}(R_2) + B_E f_{13}(R_2) = A_C f_{16}(R_2) + B_C f_{17}(R_2) \end{cases} \tag{56}$$

Combining equations (54), (55) and (56), 8 equations can be used to solve 8 unknown constants $A_P, B_P, C_1, C_0, A_E, B_E$,

A_C and B_C, as follows.

$$\begin{cases} A_P = \delta^2 V_0 \\ B_P = (\delta^1\delta^2 + V^2)V_0 \\ C_1 = \delta^3 V_0 \\ C_0 = \delta^4 V_0 \end{cases} \tag{57}$$

$$\begin{cases} A_E = (a^4\delta^2 + V^5)V_0 \\ B_E = (a^5\delta^2 + V^6)V_0 \end{cases} \tag{58}$$

$$\begin{cases} A_C = (a^9\delta^2 + V^{10})V_0 \\ B_C = (a^{10}\delta^2 + V^{11})V_0 \end{cases} \tag{59}$$

where

$$\begin{cases} \delta^1 = -[f_4(R_0) + a^1 f_6(R_0)]/[f_5(R_0) + b^1 f_6(R_0)] \\ \delta^2 = -[V^{10} f_{16}(R_3) + V^{11} f_{17}(R_3)]/[a^9 f_{16}(R_3) + a^{10} f_{17}(R_3)] \\ \delta^3 = (a^1 + b^1\delta^1)\delta^2 + (b^1 V^2 + V^1) \\ \delta^4 = -[\delta^2 f_7(R_0) + (\delta^1\delta^2 + V^2) f_8(R_0) + \delta^3 f_9(R_0)] \end{cases} \tag{60}$$

$$\begin{cases} a^1 = -[f_7(R_1) - f_7(R_0)]/[f_9(R_1) - f_9(R_0)] \\ b^1 = -[f_8(R_1) - f_8(R_0)]/[f_9(R_1) - f_9(R_0)] \\ V^1 = 1/[f_9(R_1) - f_9(R_0)] \\ V^2 = -[V^1 f_6(R_0)]/[f_5(R_0) + b^1 f_6(R_0)] \end{cases} \tag{61}$$

$$\begin{cases} a^2 = f_1(R_1) + \delta^1 f_2(R_1) + (a^1 + b^1\delta^1) f_3(R_1) \\ V^3 = V^2 f_2(R_1) + (b^1 V^2 + V^1) f_3(R_1) \\ a^3 = f_4(R_1) + \delta^1 f_5(R_1) + (a^1 + b^1\delta^1) f_6(R_1) \\ V^4 = V^2 f_5(R_1) + (b^1 V^2 + V^1) f_6(R_1) \end{cases} \tag{62}$$

$$\begin{cases} H^1 = f_{10}(R_1) f_{13}(R_1) - f_{12}(R_1) f_{11}(R_1) \\ a^4 = [a^2 f_{13}(R_1) - a^3 f_{11}(R_1)]/H^1 \\ V^5 = [V^3 f_{13}(R_1) - V^4 f_{11}(R_1)]/H^1 \\ a^5 = -[a^2 f_{12}(R_1) - a^3 f_{10}(R_1)]/H^1 \\ V^6 = -[V^3 f_{12}(R_1) - V^4 f_{10}(R_1)]/H^1 \end{cases} \tag{63}$$

$$\begin{cases} a^6 = a^4 f_{10}(R_2) + a^5 f_{11}(R_2) \\ V^7 = V^5 f_{10}(R_2) + V^6 f_{11}(R_2) \\ a^7 = a^4 f_{12}(R_2) + a^5 f_{13}(R_2) \\ V^8 = V^5 f_{12}(R_2) + V^6 f_{13}(R_2) \end{cases} \tag{64}$$

$$\begin{cases} H^2 = f_{14}(R_2) f_{17}(R_2) - f_{16}(R_2) f_{15}(R_2) \\ a^9 = [a^6 f_{17}(R_2) - a^7 f_{15}(R_2)]/H^2 \\ V^{10} = [V^7 f_{17}(R_2) - V^8 f_{15}(R_2)]/H^2 \\ a^{10} = -[a^6 f_{16}(R_2) - a^7 f_{14}(R_2)]/H^2 \\ V^{11} = -[V^7 f_{16}(R_2) - V^8 f_{14}(R_2)]/H^2 \end{cases} \tag{65}$$

Furthermore, the electrical impedance Z can be expressed as

$$Z = \frac{V(t)}{I(t)} = 1/(-j\omega 4\pi\delta^3) \tag{66}$$

In equation (66), the current $I(t)$ can be solved according to the following equation.

$$I(t) = -\frac{dQ(t)}{dt} = -\frac{d(\int_S D_r|_{r=R_1}\, dS)}{dt} = -j\omega 4\pi\delta^3 V_0 e^{j\omega t} \tag{67}$$

where S denotes the area of spherical surface at $r = R_1$.

Further, when $|Z| = 0$ and $|Z| = \infty$, the resonance frequency f_r and the anti-resonance frequency f_a can be obtained, respectively.

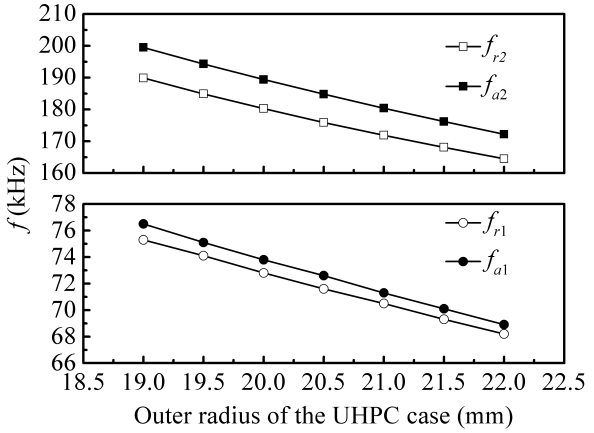

FIGURE 3. Effect of the outer radius of the UHPC case on the first and second resonance and anti-resonance frequencies.

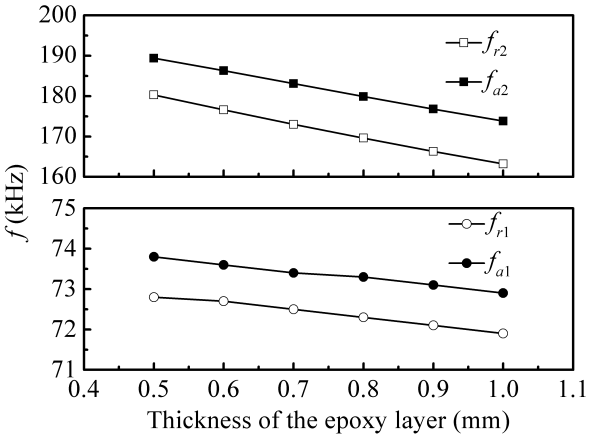

FIGURE 4. Effect of the thickness of the epoxy layer on the first and second resonance and anti-resonance frequencies.

IV. PARAMETRIC ANALYSIS

A type of embeddable spherical smart aggregate (SSA) is formed by encapsulating the radially polarized spherical piezoceremic shell with epoxy resin and spherical ultra-high performance concrete (UHPC) case, as shown in Fig. 1. The inner and outer radii of the piezoceramic shell are designed as 9.25mm and 10mm, respectively. The thickness of the epoxy layer is designed as 0.5mm. The inner and outer radii of the UHPC case are designed as 10.5mm and 20mm, respectively. The material parameters of PZT-5, Epoxy and UHPC are listed in Table 1 and Table 2, respectively. These geometrical dimensions and material parameters are adopted in the following parametric study, unless otherwise stated. Fig. 3 first displays the effect of the outer radius of the UHPC case on the vibration characteristics that include the first and second resonance and anti-resonance frequencies, which are defined as f_{r1}, f_{a1} and f_{r2}, f_{a2}, respectively. It can be found that the first and second resonance and anti-resonance frequencies are decreased with the increase in the outer radius of the UHPC case. Further, keeping the sizes of the piezoceramic shell unchanged, Fig. 4 presents the effect of the thickness

TABLE 1. Material parameters of PZT-5, PZT-5H [81], PZT-5A [81], EC-64 [82], PZT-4 [73], and $BaTiO_3$ [83].

Material types	Elastic constant ($\times 10^{10}$ N/m^2)				Piezoelectric constant (C/m^2)		Dielectric constant	Density (kg/m^3)
	c_{11}^E	c_{12}^E	c_{13}^E	c_{33}^E	e_{31}	e_{33}	$\kappa_{33}^{\varepsilon}/\varepsilon_0$	ρ_P
PZT-5	10.7	5.6	5.4	8.6	-7.2	20.4	908	7800
PZT-5H	12.6	7.95	8.41	11.7	-6.50	23.3	1470	7500
PZT-5A	12.1	7.54	7.52	11.1	-5.40	15.8	830	7750
EC-64	13.22	7.34	7.26	11.79	-4.7	16.3	644.7	7500
PZT-4	13.9	7.78	7.43	11.5	-5.2	15.1	635	7500
$BaTiO_3$	15.0	6.60	6.60	14.6	-4.35	17.5	1700	5700

$\varepsilon_0 = 8.85\times10^{-12}$ F/m , Permittivity of free space

TABLE 2. Material parameters of epoxy and UHPC.

Types	Young's modulus ($\times 10^9$ N/m^2)	Poisson's ratio	Density (kg/m^3)
Epoxy	3.89	0.38	1200
UHPC	42.8	0.19	2450

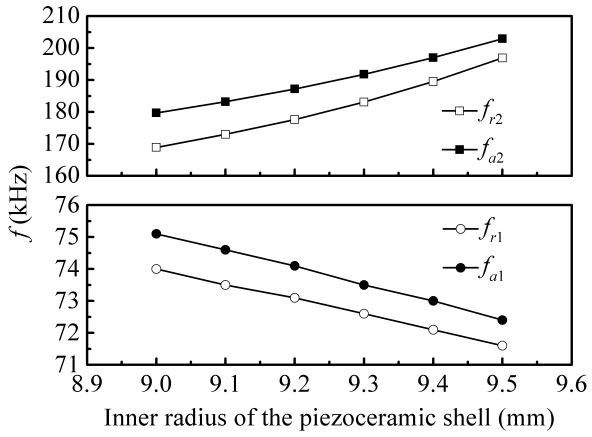

FIGURE 5. Effect of the inner radius of the piezoceramic shell on the first and second resonance and anti-resonance frequencies.

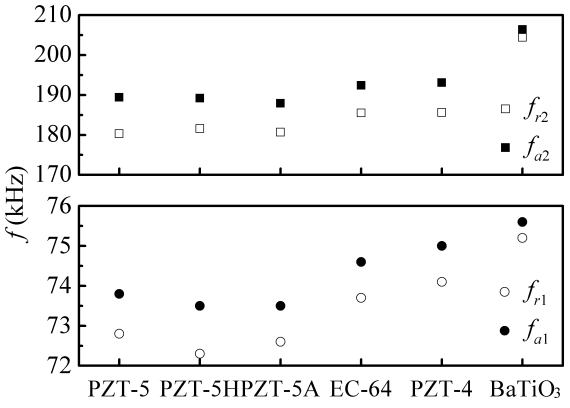

FIGURE 6. Effect of the piezoelectric material types on the first and second resonance and anti-resonance frequencies.

of the epoxy layer on the investigated transducer's vibration characteristics, indicates that the first and second resonance and anti-resonance frequencies are presenting a decreasing trend with the increase of the epoxy layer thickness. Only changing the inner radius of the piezoceramic shell, the variation of the vibration characteristics is presented in Fig. 5. It can be seen that with the increase of the inner radius of the piezoceramic shell, the first resonance and anti-resonance frequencies decrease, however, the second resonance and anti-resonance frequencies increase. The rule is similar to the result of the hollow piezoceramic sphere reported in an earlier work [80]. Furthermore, five kinds of commonly used

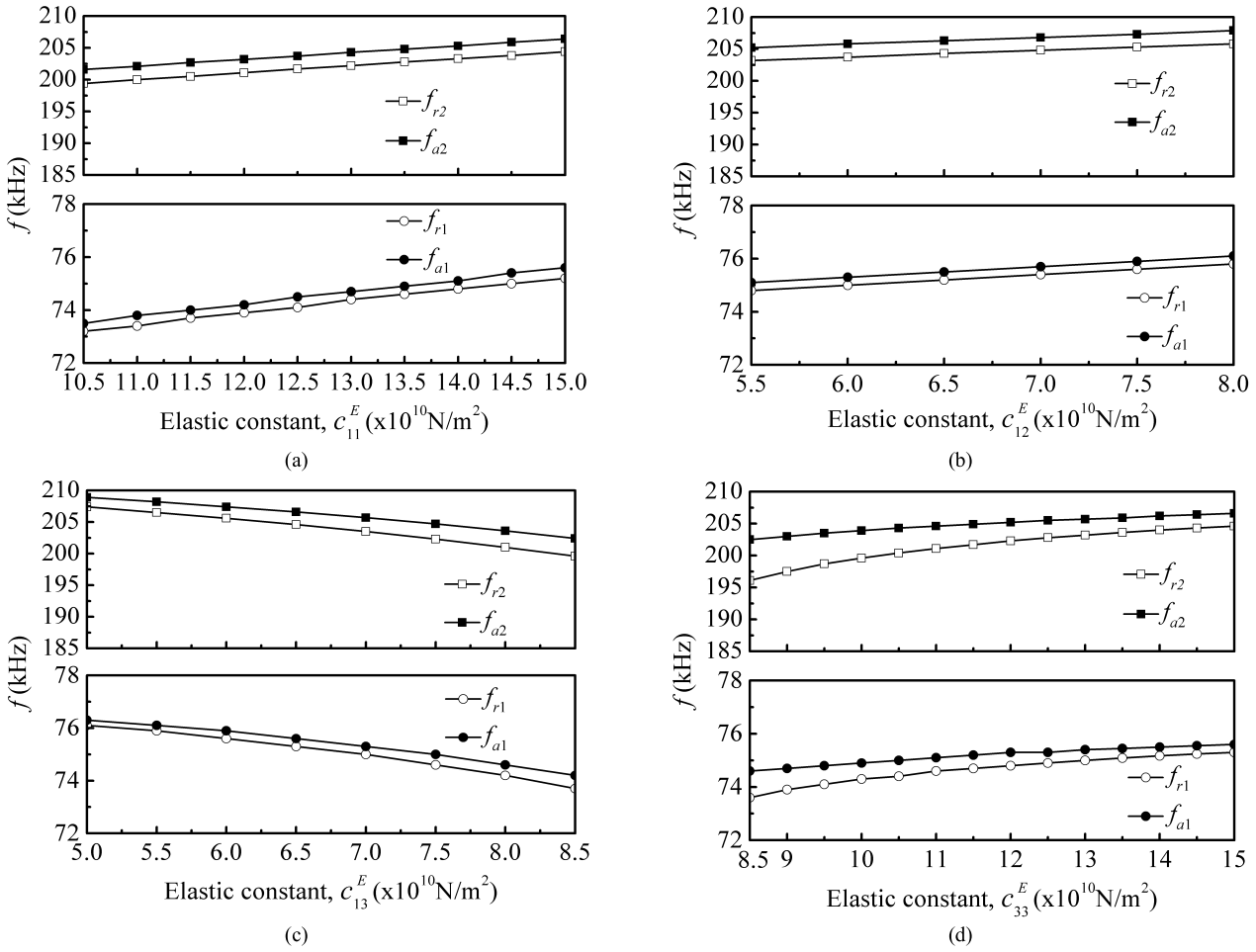

FIGURE 7. Effect of the elastic constants of piezoelectric material c_{11}^E, c_{12}^E, c_{13}^E and c_{33}^E on the first and second resonance and anti-resonance frequencies.

piezoelectric materials, such as PZT-5H [81], PZT-5A [81], EC-64 [82], PZT-4 [73], and $BaTiO_3$ [83], are introduced to discuss the effect of the piezoelectric material type on the vibration characteristics. Their material parameters can be found in Table 1. Corresponding results are plotted in Fig. 6. It can be observed that the SSA with $BaTiO_3$ has the maximum first and second resonance and anti-resonance frequencies, and the difference of the vibration characteristics between the adopted PZT-5 used in this paper and the standard PZT-5H and PZT-5A is relatively small. The discrepancy is dominated by the piezoelectric material parameters. In order to distinguish clearly which piezoelectric material parameter is affecting mainly the result, the variation in the given material property is introduced to evaluate the effect to understand what properties should be prioritized in design. The material parameters of $BaTiO_3$ are adopted in the following analysis, unless otherwise stated. Figs. 7∼10 highlight the effects of the elastic constants c_{11}^E, c_{12}^E, c_{13}^E, c_{33}^E, the piezoelectric constants e_{31}, e_{33}, the dielectric constant $\kappa_{33}^{\varepsilon}/\varepsilon_0$, the density ρ_P on the first and second resonance and anti-resonance frequencies. From Fig. 7, it can be found that these two groups of frequencies increase with the increases of the elastic constants c_{11}^E, c_{12}^E, c_{33}^E, while decrease with the increase of the elastic constant c_{13}^E. From Fig. 8, it can be found that these frequencies are hardly affected by the increases of the piezoelectric constants e_{31}, e_{33} although they present an increasing trend. From Figs. 9∼10, it can be seen that these frequencies are decreased with the increasing dielectric constant $\kappa_{33}^{\varepsilon}/\varepsilon_0$ and density ρ_P, and the density has the greater influence. In general, the effects of piezoelectric constants e_{31}, e_{33} can be ignored in designing the resonance frequencies of the SSA. Selecting the greater elastic constants c_{11}^E, c_{12}^E, c_{33}^E, the smaller elastic constant c_{13}^E, dielectric constant $\kappa_{33}^{\varepsilon}/\varepsilon_0$ and density ρ_P can obtain effectively the higher resonance frequencies, and vice versa.

V. VALIDATION

In this section, some special cases in the literature are firstly used to validate the derived theoretical solution. Then, an ANSYS numerical simulation and an experimental study are conducted to verify the reliability of the proposed model of the SSA.

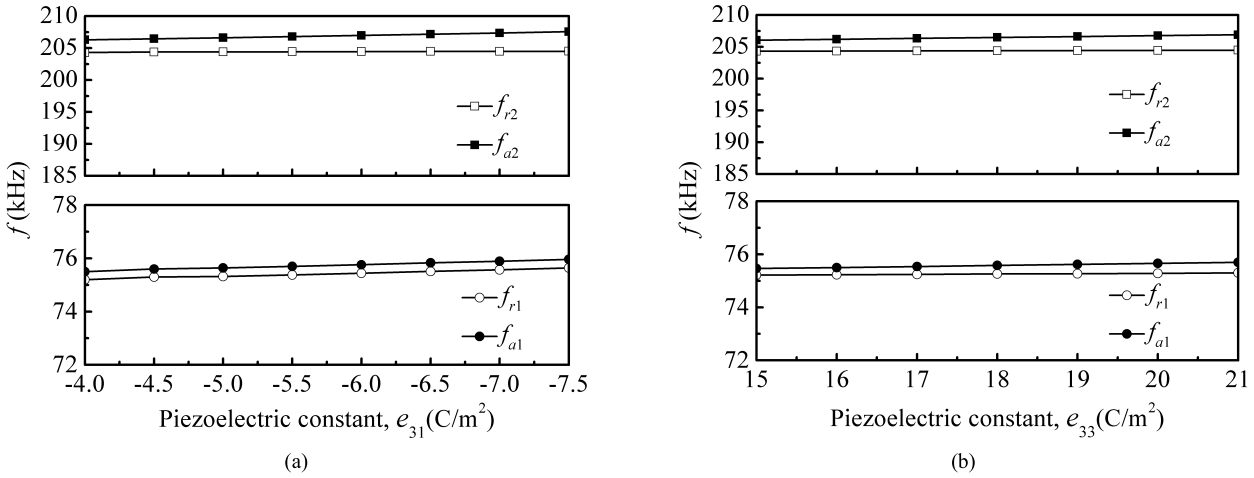

FIGURE 8. Effect of the piezoelectric constants of piezoelectric material e_{31} and e_{33} on the first and second resonance and anti-resonance frequencies.

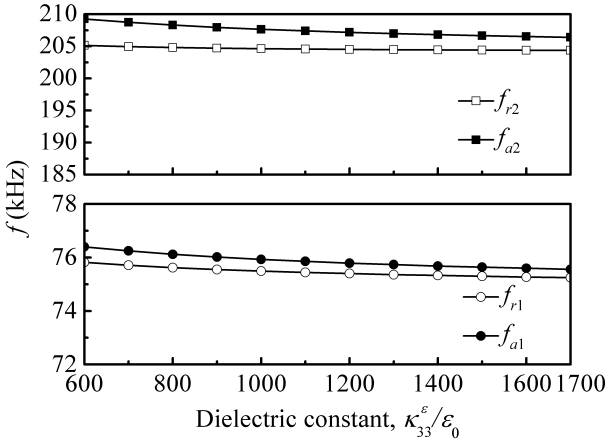

FIGURE 9. Effect of the dielectric constant of piezoelectric material $\kappa_{33}^{\varepsilon}/\varepsilon_0$ on the first and second resonance and anti-resonance frequencies.

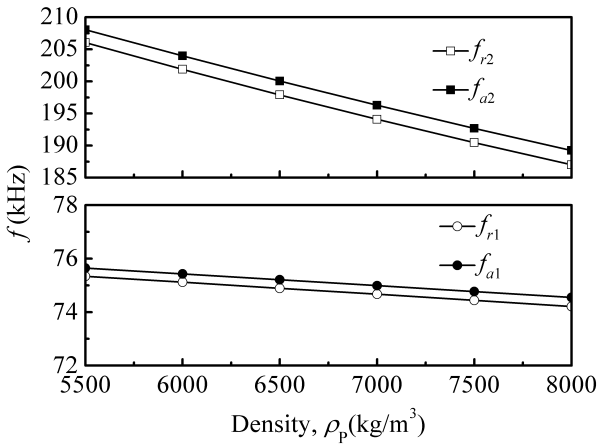

FIGURE 10. Effect of the density of piezoelectric material ρ_p on the first and second resonance and anti-resonance frequencies.

A. SOME SPECIAL CASES IN THE LITERATURE

In this section, two comparisons are presented to validate the derived theoretical solution. The present solution can be reduced approximately to the solution of the single layer piezoceramic shell when the thicknesses of the epoxy layer and the UHPC layer tend to zero, which is used to compare with the previous work. In Kim *et al.*'s work [74], the radial vibration characteristics of the spherical transducer is studied by using the method eliminating the terms including e_{31} from the governing equations, the finite element analysis with commercial package ANSYS and the experimental method. The fabricated spherical transducer is composed of two hemispherical transducers, and one of them has a wire hole of 3mm diameter. The piezoelectric material is selected as PZT-5A, as shown in Table 1. Comparisons of the first resonance frequencies obtained by the present method and the methods in Kim *et al.*'s work [74] is presented in Table 3. Qualitatively, these frequencies agree reasonably well. The present theoretical results are larger than the theoretical, experimental and FEM values in Kim *et al.*'s work. The reason for the discrepancy between the present theoretical results, and the experimental and FEM values in Kim *et al.*'s work can be explained as follow. In the theory, the perfect sphere shell is considered, while it is actually formed by two hemispherical shells and one of them has a wire hole, which result in a decrease in the whole stiffness of the transducer. The reason for the discrepancy between the present theoretical results and the theoretical ones in Kim *et al.*'s work can be explained as follow. The simplified method eliminating the terms including e_{31} from the governing equations will reduce the structural stiffness in the theoretical calculation and results in the lower frequencies. In Drenkow and Long's work [80], the frequency equation is specialized to investigate the radial vibration of a barium-titanate ($BaTiO_3$) thick sphere shell, and the first three frequencies are analyzed by tabulating. The frequency equation is established when the inner and

TABLE 3. Comparisons of the first resonance frequencies obtained by the present method and the methods in Kim *et al.*'s work [74].

No.	Model	R_0 (mm)	R_1 (mm)	R_2 (mm)	R_3 (mm)	Method	f_{r1}(kHz)
1	Present	10.7	12.7	12.701	12.702	Theory	78
	[74]	10.7	12.7	~	~	Theory	58.9
						FEM(With a hole)	68
						FEM(Without a hole)	69
						Experiment	64
2	Present	4.76	6.35	6.3501	6.3502	Theory	165.3
	[74]	4.76	6.35	~	~	Theory	125
						FEM(With a hole)	139
						FEM(Without a hole)	145
						Experiment	135

FEM denotes a commercial software ANSYS.

TABLE 4. Comparisons of the first three anti-resonance frequencies obtained by the present method and the method in Drenkow and Long's work [80].

No.	Model	R_0(mm)	R_1(mm)	R_2(mm)	R_3(mm)	Method	f_{a1}(kHz)	f_{a2}(kHz)	f_{a3}(kHz)
3	Present	95	105	105.01	105.02	Theory	12.439	270.28	540.06
	[80]	95	105	~	~	Theory	12.446	271.31	541.69
4	Present	70	130	130.01	130.02	Theory	12.748	47.285	91.138
	[80]	70	130	~	~	Theory	12.742	47.344	91.153

outer surfaces of the shell are stress free and the net surface charge density at the outer radius is zero. Comparisons of the first three anti-resonance frequencies obtained by the present method and the method in Drenkow and Long's work [80] are presented in Table 4. The obtained results from the different methods show good agreements, which further validate the proposed theoretical solution.

B. ANSYS NUMERICAL SIMULATION

In this section, the present solution is compared to the ANSYS simulation results of the SSA. In the simulation, to guarantee precision and improve computation efficiency, one-eighth of the SSA is modeled in spherical coordinate system by using ANSYS R17.1 because of the symmetry of the perfect spherical structure, as shown in Fig. 11. The element Solid 5 is chosen for the piezoelectric part. The element Solid 185 is chosen for the epoxy and UHPC parts. The amount of elements and nodes are 26208 and 28825, respectively. At the inner surface of the PZT shell, all the voltage degrees of freedom (DOFs) of the negative electrode are coupled, and $V_0 = 0$V is applied. At the outer surface of the PZT shell, all the voltage degrees of freedom (DOFs) of the positive electrode are coupled, and $V_0 = 1$V is applied. The analysis type is selected as harmonic, and the harmonic frequency range is 0~200 kHz. The computation is carried out in 100Hz steps. The simulated impedance is plotted in Fig. 12. In addition,

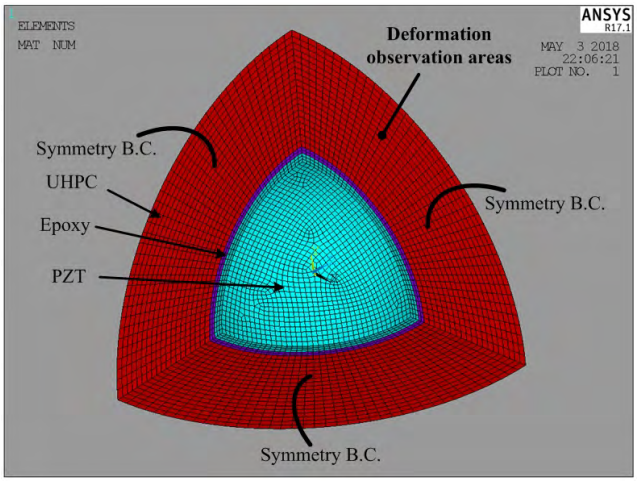

FIGURE 11. Finite element model of the SSA.

the theoretical impedance is also addressed in Fig. 12. It can be found that the ANSYS simulation results are in reasonably good agreement with the theoretical predictions. Further, the theoretical and simulated first and second resonance and anti-resonance frequencies are compared in Table 5. The relative errors between the theoretical values and the simulated ones for the first resonance frequency, the first anti-resonance frequency, the second resonance

TABLE 5. Comparisons between the calculated, simulated and experimental frequencies.

Frequencies (kHz)		f_{r1}	f_{a1}	f_{r2}	f_{a2}
Theory		72.8	73.8	180.3	189.4
ANSYS		70.7	73.8	180.4	189.5
Error 1 (%)		2.88	0	-0.06	-0.05
Experiment [62]	SSA-1	58.5	65.3	107.5	129.3
	SSA-2	57.0	62.5	117.5	130.5
	SSA-3	53.3	56.5	109.0	129.3
Error 2 (%)	SSA-1	19.64	11.52	40.38	31.73
	SSA-2	21.70	15.31	34.83	31.10
	SSA-3	26.79	23.44	39.55	31.73

Error 1 = (Theory-ANSYS)/Theory; Error 2 = (Theory-Experiment)/Theory

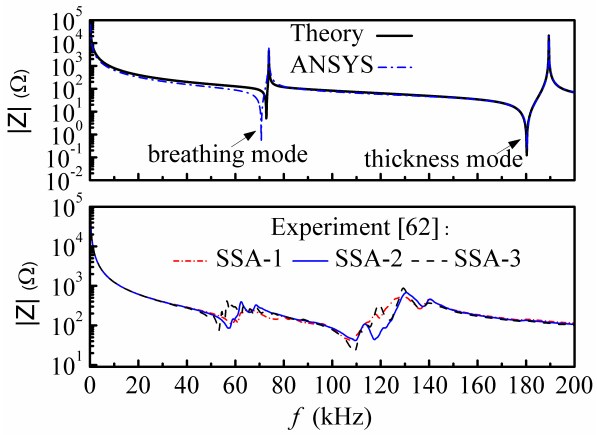

FIGURE 12. Theoretical, simulated and experimental impedance spectra.

frequency and the second anti-resonance frequency, are 2.88 %, 0, −0.06 % and −0.05 %, respectively. The above comparative results validate the reliability of the theoretical solution.

Further, to understand clearly which vibration mode is being used, the displacement fields at the first resonance frequency and the second resonance frequency, shown in Figs. 13 and 14, are given for identifying the vibration mode shapes. Similarly to the vibration modes of the BBs [56] (A type of miniature piezoelectric hollow sphere transducers are called ''BBs'' or ''BB transducers'' due to the similarity to ball bearings and to the spherical pellets used in air rifles in shape and size [61], which have potential applications include ultrasonic imaging, hydrophones and nondestructive testing), the first mode is a volumetric expansion and contraction of the SSA, the so-called breathing mode that is mainly utilizes e_{31} coefficient of piezoelectricity and the second mode is identified as the thickness mode that mainly utilizes e_{33} coefficient of piezoelectricity.

C. EXPERIMENTAL VALIDATION

In this section, the present solution is compared to the experimental results of the SSA. The experimental setup is shown in Fig. 15 [62]. The test system includes an Agilent 4294A Precision Impedance Analyzer for measurement and a laptop for data acquisition. In the experiment, the SSA is held by a support to realize approximately free boundary conditions. The measured impedance spectra of three fabricated SSAs are plotted in Fig. 12, and the corresponding resonance and anti-resonance frequencies are also addressed in Table 5. It can be observed that the theoretical and experimental impedance spectra have a good consistency. Qualitatively, the theoretical resonance and anti-resonance frequencies are larger than the experimental values. For the first resonance and anti-resonance frequencies, the discrepancy is relatively small; however, for the second resonance and anti-resonance frequencies, this discrepancy is very significant. The most possible reason for the difference between the theoretical and experimental results is that the PZT layer and the UHPC layer are considered as the perfect sphere shells in the theoretical model, while these layers are actually fabricated from two hemispherical shells and one of them has a wire hole, which lead to a decrease in the whole stiffness of the SSA. In [62], a three-dimensional finite element model of the SSA with a wire hole of 2mm diameter was modeled by using ABAQUS software. The simulated first resonance and anti-resonance frequencies are 54.4 kHz and 57.1 kHz, respectively. The simulated second resonance and anti-resonance frequencies are in the range of 130∼150 kHz. These frequencies are smaller than the theoretical results but very close to the experimental ones, which further prove the reason. In general, the proposed model can still help to understand the vibration characteristics of the SSA, which is helpful to design the working frequencies range of the SSA.

D. DISCUSSION

In practical applications of health monitoring of civil infrastructures, the SSAs are embedded at pre-determined locations inside the civil engineering structures and combine an active-sensing approach to implement the monitoring. In this method, one SSA is usually used as an actuator to generate

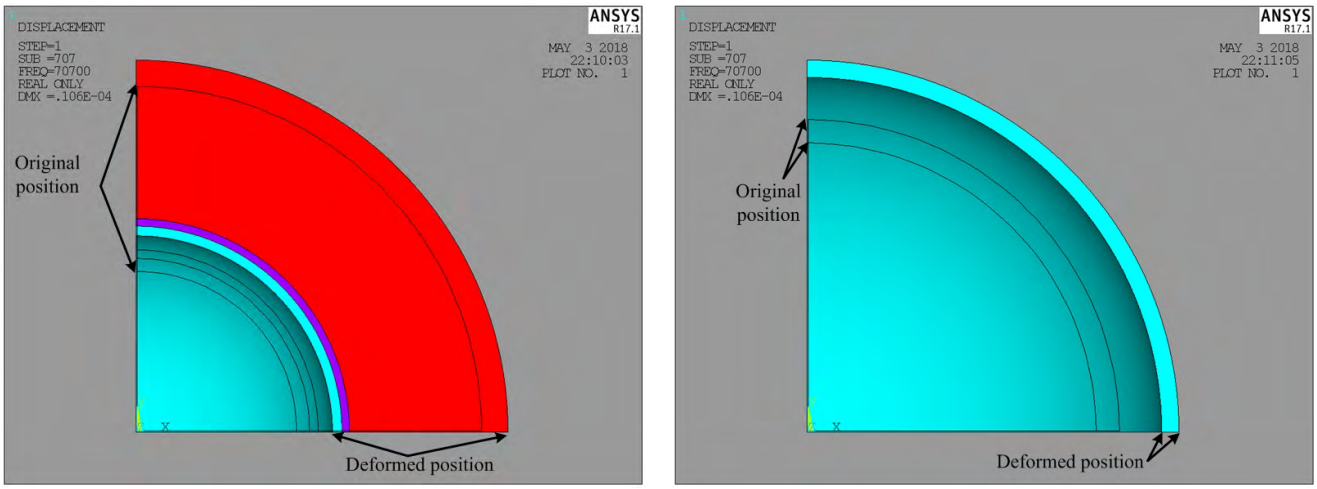

FIGURE 13. Displacement field of (a) the SSA and (b) the PZT part at the first resonance frequency (Solid line corresponds to the original position and colored area to the deformed position.)

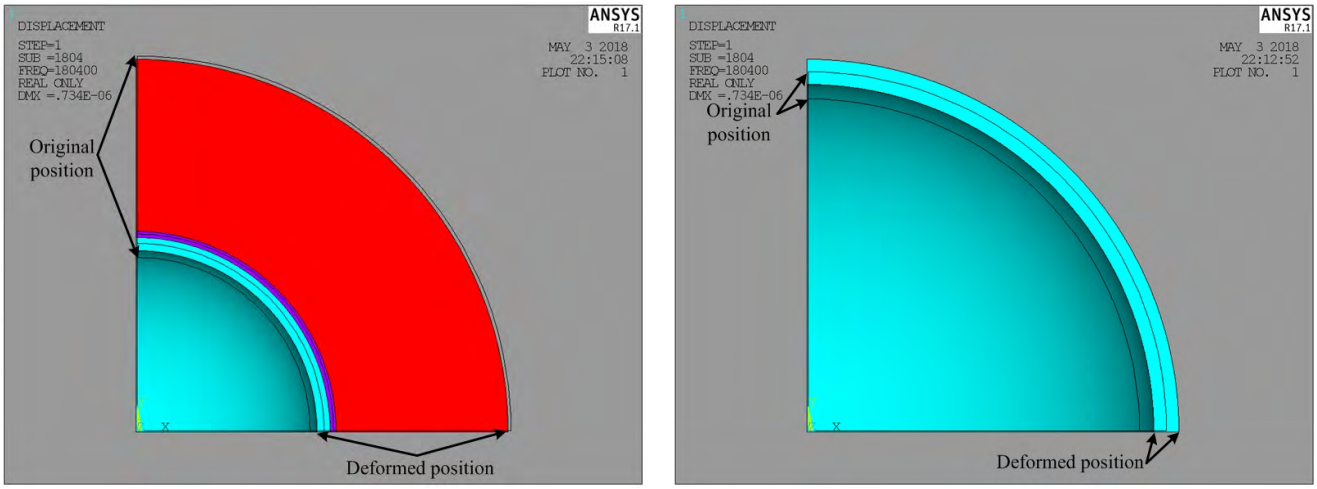

FIGURE 14. Displacement field of (a) the SSA and (b) the PZT part at the second resonance frequency (Solid line corresponds to the original position and colored area to the deformed position.)

guided sinusoidal waves with a constant frequency or a sweep frequency. Simultaneously, the other SSAs act as sensors to collect the signal from the actuators. Since the most mechanical or structural background noise and ambient excitation are in the low frequency range (<100 Hz) [41], the relative high frequency range from a few hundreds of Hz to a few hundreds of kHz is usually selected to minimize environmental noise and disturbance during the measurement. Therefore, the SSA was designed aiming the first resonant frequencies at the order of 100 kHz, while not at the order of 1 Hz, the resonant frequency range of a typical civil infrastructure.

As mentioned above, an SSA is usually used as an actuator to generate guided sinusoidal waves with a constant frequency or a sweep frequency. The frequency can be the resonant frequencies, and or not. Therefore, it is not indispensable that the SSA must work at the resonant mode. However, for the sake of receiving desirable signal response, it is essential to carefully select appropriate frequency ranges of the excitation wave. As we all known, the excited energy near the resonant frequencies is larger than other frequencies. Therefore, predicting the resonant frequencies of the SSA to help the selection of the excitation frequency or frequency range can significantly improve the efficiency of the monitoring system and increase its reliability and accuracy.

In addition, it should be noted that the present model is established in the free field, whereas the practical application requires the device to be embedded in the civil engineering structures that will constrain the motion of the external surface and significantly affect the transducer response. Future effects will introduce the imperfect factors induced by the hemispherical shells and the wire hole, as well as the boundary conditions affected by the host structures into the model

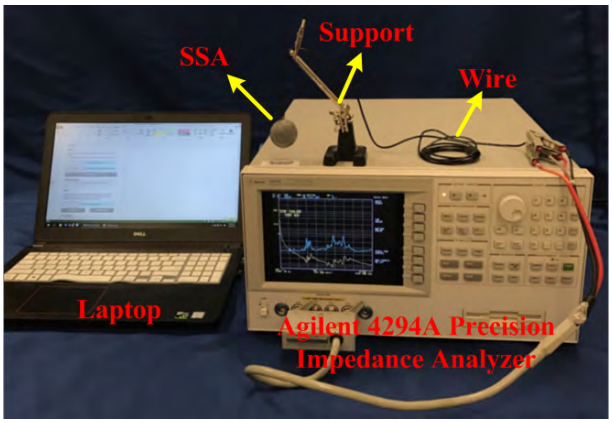

FIGURE 15. Photograph of experimental setup [62].

to increase the accuracy and practicability, which is expected to be used in structural elements under the cyclic loads for definition of damage indices for seismic actions, and also can be used in bridge columns to control the vibrations in structure.

VI. CONCLUSION

This article proposed a simplified theoretical model to investigate the vibration characteristics of the SSA based on the linear theory of piezoelasticity, and performed a series of comparisons with some special cases, numerical simulation results and experimental data to verify its reliability. The comparative results showed that the proposed model can approximately predict the vibration characteristics of the SSA, especially for the first resonance and anti-resonance frequencies. However, by simplifying the actual SSA that was fabricated from two hemispherical shells with a wire hole as the perfect sphere shell, the whole stiffness of the SSA was strengthened in the computation. Quantitatively, the obtained theoretical results are larger than the experimental ones.

By employing the proposed model, the parametric analysis was performed to evaluate the effects of the geometrical dimensions, the piezoelectric material types and the piezoelectric material parameters on the first and second resonance and anti-resonance frequencies. Some design recommendations can be suggested. A smaller outer radius of the UHPC case and a thinner epoxy layer effectively result in higher resonance frequencies. On the other hand, a larger inner radius of the piezoceramic shell lead to lower first resonance and anti-resonance frequencies, and higher second resonance and anti-resonance frequencies. Selecting different piezoelectric material types and piezoelectric material parameters can generate different vibration characteristics. Among PZT-5, PZT-5H, PZT-5A, EC-64, PZT-4 and $BaTiO_3$, the SSA with $BaTiO_3$ has the maximum first and second resonance and anti-resonance frequencies, and the SSAs with PZT-5, PZT-5H and PZT-5A have the relatively smaller, approximately equal resonant frequencies. In addition, greater elastic constants c_{11}^E, c_{12}^E, c_{33}^E, and smaller elastic constant c_{13}^E, dielectric constant $\kappa_{33}^{\varepsilon}/\varepsilon_0$ and density ρ_P lead to higher resonance frequencies.

This study has some valuable findings on the vibration characteristics of the SSA; however, there are still some limitations. The present model is established in the free field, whereas practical applications require the device to be embedded in the civil engineering structures that will constrain the motion of the external surface and significantly affect the transducer response. The present model simplified the actual SSA that was fabricated from two hemispherical shells with a wire hole as a perfect sphere shell, while these two defects actually existed that will reduce the whole stiffness of the SSA. Future studies will focus on the improvement of the model and the SSA-based health monitoring of civil engineering structures. Firstly, the imperfect factors induced by the hemispherical shells and the wire hole, as well as the boundary conditions affected by the host structures will be introduced to the modeling process to increase the accuracy and practicability.

ACKNOWLEDGMENT

(Qingzhao Kong is co-first author.)

REFERENCES

[1] I. H. Grinberg, N. Maccabi, A. Kassie, and D. Elata, "A piezoelectric twisting beam actuator," *J. Microelectromech. Syst.*, vol. 26, no. 6, pp. 1279–1286, Dec. 2017.

[2] P. C.-P. Chao and C.-Y. Shen, "Dynamic modeling and experimental verification of a piezoelectric part feeder in a structure with parallel bimorph beams," *Ultrasonics*, vol. 46, no. 3, pp. 205–218, Jun. 2007.

[3] D. Y. Xu, S. Banerjee, Y. Wang, S. Huang, and X. Cheng, "Temperature and loading effects of embedded smart piezoelectric sensor for health monitoring of concrete structures," *Construction Build. Mater.*, vol. 76, pp. 187–193, Feb. 2015.

[4] P. C.-P. Chao, "Energy harvesting electronics for vibratory devices in self-powered sensors," *IEEE Sensors J.*, vol. 11, no. 12, pp. 3106–3121, Dec. 2011.

[5] S. R. Anton and H. A. Sodano, "A review of power harvesting using piezoelectric materials (2003–2006)," *Smart Mater. Struct.*, vol. 16, no. 3, pp. R1–R21, 2007.

[6] L. Tang, Y. Yang, and C. K. Soh, "Toward broadband vibration-based energy harvesting," *J. Int. Mater. Syst. Struct.*, vol. 21, no. 18, pp. 1867–1897, Dec. 2010.

[7] Y. Li, Z. Çelik-Butler, and D. P. Butler, "An integrated piezoelectric zinc oxide nanowire micro-energy harvester," *Nano Energy*, vol. 26, pp. 456–465, Aug. 2016.

[8] B. P. Nabar, Z. Çelik-Butler, and D. P. Butler, "Piezoelectric ZnO nanorod carpet as a NEMS vibrational energy harvester," *Nano Energy*, vol. 10, pp. 71–82, Nov. 2014.

[9] J. Yang, "Piezoelectric transformer structural modeling—A review," *IEEE Trans. Ultrason., Ferroelect., Freq. Control*, vol. 54, no. 6, pp. 1154–1170, Jun. 2007.

[10] S. Lele, R. Sobot, and T. Sidhu, "Piezoelectric transformer based disturbance monitoring methodology for high-voltage power supply lines," *IEEE Sensors J.*, vol. 14, no. 5, pp. 1425–1434, May 2014.

[11] H. J. Lee and S. Zhang, "Design of low-loss 1-3 piezoelectric composites for high-power transducer applications," *IEEE Trans. Ultrason., Ferroelect., Freq. Control*, vol. 59, no. 9, pp. 1969–1975, Sep. 2012.

[12] C. Dumoulin and A. Deraemaeker, "A study on the performance of piezoelectric composite materials for designing embedded transducers for concrete assessment," *Smart Mater. Struct.*, vol. 27, no. 3, p. 035008, 2018.

[13] H. Gu, Y. L. Mo, and G. Song, "Recent progress in smart aggregate-based structural health monitoring of civil structures," in *Proc. Innov. Technol. Struct. Health Monit. Symp. ASCE Earth Space Conf.*, vol. 2010, pp. 14–17.

[14] G. Song, H. Gu, and Y.-L. Mo, "Smart aggregates: Multi-functional sensors for concrete structures—A tutorial and a review," *Smart Mater. Struct.*, vol. 17, no. 3, p. 033001, 2008.
[15] H. Gu, G. Song, H. Dhonde, Y. L. Mo, and S. Yan, "Concrete early-age strength monitoring using embedded piezoelectric transducers," *Smart Mater. Struct.*, vol. 15, no. 6, pp. 1837–1845, 2006.
[16] A. Laskar, H. Gu, Y. L. Mo, and G. Song, "Progressive collapse of a two-story reinforced concrete frame with embedded smart aggregates," *Smart Mater. Struct.*, vol. 18, no. 7, p. 075001, 2009.
[17] T. Liu, Y. Huang, D. Zou, J. Teng, and B. Li, "Exploratory study on water seepage monitoring of concrete structures using piezoceramic based smart aggregates," *Smart Mater. Struct.*, vol. 22, no. 6, p. 065002, 2013.
[18] R. L. Wang, H. Gu, Y. L. Mo, and G. Song, "Proof-of-concept experimental study of damage detection of concrete piles using embedded piezoceramic transducers," *Smart Mater. Struct.*, vol. 22, no. 4, p. 042001, 2013.
[19] C. Dumoulin, G. Karaiskos, J.-Y. Sener, and A. Deraemaeker, "Online monitoring of cracking in concrete structures using embedded piezoelectric transducers," *Smart Mater. Struct.*, vol. 23, no. 11, p. 115016, 2014.
[20] C. Dumoulin and A. Deraemaeker, "Real-time fast ultrasonic monitoring of concrete cracking using embedded piezoelectric transducers," *Smart Mater. Struct.*, vol. 26, no. 10, p. 104006, 2017.
[21] W.-I. Liao, C. H. Lin, J. S. Hwang, and G. Song, "Seismic health monitoring of RC frame structures using smart aggregates," *Earthq. Eng. Eng. Vib.*, vol. 12, no. 1, pp. 25–32, Mar. 2013.
[22] B. Xu, T. Zhang, G. Song, and H. Gu, "Active interface debonding detection of a concrete-filled steel tube with piezoelectric technologies using wavelet packet analysis," *Mech. Syst. Signal Process.*, vol. 36, no. 1, pp. 7–17, Mar. 2013.
[23] B. Xu, G. Song, and Y. L. Mo, "Embedded piezoelectric lead-zirconate-titanate-based dynamic internal normal stress sensor for concrete under impact," *J. Intell. Mater. Syst. Struct.*, vol. 28, no. 19, pp. 2659–2674, 2017.
[24] C. Dumoulin, G. Karaiskos, J. Carette, S. Staquet, and A. Deraemaeker, "Monitoring of the ultrasonic P-wave velocity in early-age concrete with embedded piezoelectric transducers," *Smart Mater. Struct.*, vol. 21, no. 4, p. 047001, 2012.
[25] D. Ai, H. Zhu, H. Luo, and C. Wang, "Mechanical impedance based embedded piezoelectric transducer for reinforced concrete structural impact damage detection: A comparative study," *Construction Building Mater.*, vol. 165, pp. 472–483, Mar. 2018.
[26] Z.-X. Li, X.-M. Yang, and Z. Li, "Application of cement-based piezoelectric sensors for monitoring traffic flows," *J. Trans. Eng.*, vol. 132, no. 7, pp. 565–573, 2006.
[27] X. M. Yang, Z. X. Li, Y. Ding, and Z. J. Li, "Test on sensor effect of cement matrix piezoelectric composite," *Trans. Tianjin Univ.*, vol. 11, no. 2, pp. 133–136, 2005.
[28] Z. J. Li, D. Zhang, and K. R. Wu, "Cement matrix 2-2 piezoelectric composite—Part 1. Sensory effect," *Mater. Struct.*, vol. 34, no. 8, pp. 506–512, Oct. 2001.
[29] D. Zhang, Z. Li, and K.-R. Wu, "2-2 piezoelectric cement matrix composite: Part II. Actuator effect," *Cement Concrete Res.*, vol. 32, no. 5, pp. 825–830, May 2002.
[30] D. Xu, X. Cheng, S. Huang, and M. Jiang, "Electromechanical properties of 2-2 cement based piezoelectric composite," *Current Appl. Phys.*, vol. 9, no. 4, pp. 816–819, 2009.
[31] D. Xu, X. Cheng, S. F. Huang, and M. H. Jiang, "Effect of cement matrix and composite thickness on properties of 2-2 type cement-based piezoelectric composites," *J. Compos. Mater.*, vol. 45, no. 20, pp. 2083–2089, 2011.
[32] S. Hou, H. B. Zhang, and J. P. Ou, "A PZT-based smart aggregate for compressive seismic stress monitoring," *Smart Mater. Struct.*, vol. 21, no. 10, p. 105035, 2012.
[33] S. Hou, H. B. Zhang, and J. P. Ou, "A PZT-based smart aggregate for seismic shear stress monitoring," *Smart Mater. Struct.*, vol. 22, no. 6, p. 065012, 2013.
[34] Q. Kong, S. Hou, Q. Ji, Y. L. Mo, and G. Song, "Very early age concrete hydration characterization monitoring using piezoceramic based smart aggregates," *Smart Mater. Struct.*, vol. 22, no. 8, p. 085025, Jul. 2013.
[35] Q. Kong, R. Wang, G. Song, Z. Yang, and B. Still, "Monitoring the soil freeze-thaw process using piezoceramic-based smart aggregate," *J. Cold Regions Eng.*, vol. 28, no. 2, p. 06014001, 2014.
[36] Q. Kong and G. Song, "A comparative study of the very early age cement hydration monitoring using compressive and shear mode smart aggregates," *IEEE Sensors J.*, vol. 17, no. 2, pp. 256–260, Jan. 2017.
[37] D. Zou, T. Liu, Y. Huang, F. Zhang, C. Du, and B. Li, "Feasibility of water seepage monitoring in concrete with embedded smart aggregates by P-wave travel time measurement," *Smart Mater. Struct.*, vol. 23, no. 6, p. 067003, 2014.
[38] J. Zhu, S. C. M. Ho, Q. Kong, D. Patil, Y.-L. Mo, and G. Song, "Estimation of impact location on concrete column," *Smart Mater. Struct.*, vol. 26, no. 5, p. 055037, 2017.
[39] H. Zhang, S. Hou, and J. Ou, "Feasibility of SA–based concrete seismic stress monitoring for high-strength concrete," *J. Intell. Mater. Syst. Struct.*, vol. 28, no. 17, pp. 2428–2436, 2017.
[40] F. Qin, Q. Kong, M. Li, Y. L. Mo, G. Song, and F. Fan, "Bond slip detection of steel plate and concrete beams using smart aggregates," *Smart Mater. Struct.*, vol. 24, no. 11, p. 115039, 2015.
[41] Q. Feng, Q. Kong, and G. Song, "Damage detection of concrete piles subject to typical damage types based on stress wave measurement using embedded smart aggregates transducers," *Measurement*, vol. 88, no. 2, pp. 345–352, Jun. 2016.
[42] S. Taghavipour, S. Kharkovsky, W.-H. Kang, B. Samali, and O. Mirza, "Detection and monitoring of flexural cracks in reinforced concrete beams using mounted smart aggregate transducers," *Smart Mater. Struct.*, vol. 26, no. 10, p. 104009, 2017.
[43] Q. Kong, Q. Feng, and G. Song, "Water presence detection in a concrete crack using smart aggregates," *Int. J. Smart Nano Mater.*, vol. 6, no. 3, pp. 149–161, 2015.
[44] C. Du, D. Zou, T. Liu, and H. Lv, "An exploratory experimental and 3D numerical investigation on the effect of porosity on wave propagation in cement paste," *Measurement*, vol. 122, pp. 611–619, Jul. 2018, doi: 10.1016/j.measurement.2017.10.025.
[45] G. Du, J. Zhang, J. Zhang, and G. Song, "Experimental study on stress monitoring of sand-filled steel tube during impact using piezoceramic smart aggregates," *Sensors*, vol. 17, no. 8, p. 1930, 2017.
[46] Q. Feng, J. Cui, Q. Wang, S. Fan, and Q. Kong, "A feasibility study on real-time evaluation of concrete surface crack repairing using embedded piezoceramic transducers," *Measurement*, vol. 17, no. 8, pp. 591–596, Jul. 2018, doi: 10.1016/j.measurement.2017.09.015.
[47] T. Jiang, Q. Kong, D. Patil, Z. Luo, L. Huo, and G. Song, "Detection of debonding between fiber reinforced polymer bar and concrete structure using piezoceramic transducers and wavelet packet analysis," *IEEE Sensors J.*, vol. 17, no. 7, pp. 1992–1998, Apr. 2017.
[48] T. Jiang *et al.*, "Monitoring of corrosion-induced degradation in pre-stressed concrete structure using embedded piezoceramic-based transducers," *IEEE Sensors J.*, vol. 17, no. 18, pp. 5823–5830, Sep. 2017.
[49] Q. Kong, H. Chen, Y.-L. Mo, and G. Song, "Real-time monitoring of water content in sandy soil using shear mode piezoceramic transducers and active sensing—A feasibility study," *Sensors*, vol. 17, no. 10, p. 2395, 2017.
[50] D. Zou, T. Liu, A. Yang, Y. Zhao, and C. Du, "A primary study on the performance of piezoceramic based smart aggregate under various compressive stresses," *Smart Mater. Struct.*, vol. 26, no. 10, p. 107003, 2017.
[51] D. Zou, T. Liu, G. Qiao, Y. Huang, and B. Li, "An experimental study on the performance of piezoceramic-based smart aggregate in water environment," *IEEE Sensors J.*, vol. 14, no. 4, pp. 943–944, 2014.
[52] D. Zou, T. Liu, C. Liang, Y. Huang, F. Zhang, and C. Du, "An experimental investigation on the health monitoring of concrete structures using piezoelectric transducers at various environmental temperatures," *J. Intell. Mater. Syst. Struct.*, vol. 26, no. 8, pp. 1028–1034, 2015.
[53] T. Liu, D. Zou, C. Du, and Y. Wang, "Influence of axial loads on the health monitoring of concrete structures using embedded piezoelectric transducers," *Struct. Health Monit.*, vol. 16, no. 2, pp. 202–214, 2017.
[54] L. Wang, L. Qin, W. Li, B. Zhang, Y. Lu, and G. Li, "Analysis on radial vibration of a stack of piezoelectric shells," *Ceram. Int.*, vol. 41, no. S1, pp. S856–S860, Jul. 2015.
[55] J. George, D. D. Ebenezer, and S. K. Bhattacharyya, "Receiving sensitivity and transmitting voltage response of a fluid loaded spherical piezoelectric transducer with an elastic coating," *J. Acoust. Soc. Amer.*, vol. 128, no. 4, pp. 1712–1720, 2010.
[56] S. Alkoy, "Piezoelectric hollow sphere transducers: The 'BBs,'" Ph.D. dissertation, Dept. Mater. Sci. Eng., Pennsylvania State Univ., State College, PA, USA, 1999.
[57] S. Alkoy, A. Dogan, A.-C. Hladky, P. Langlet, J. K. Cochran, and N. E. Newnham, "Miniature piezoelectric hollow sphere transducers (BBs)," *IEEE Trans. Ultrason., Ferroelectr., Freq. Control*, vol. 44, no. 5, pp. 1067–1076, Sep. 1997.

[58] S. Alkoy, R. J. Meyer, Jr., W. J. Hughes, J. K. Cochran, Jr., and R. E. Newnham, "Design, performance and modeling of piezoceramic hollow-sphere microprobe hydrophones," *Meas. Sci. Technol.*, vol. 20, no. 9, p. 095204, 2009.

[59] J. Hu, Z. Qiu, and T. Su, "Axisymmetric vibrations of a viscous-fluid-filled piezoelectric spherical shell and the associated radiation of sound," *J. Sound Vib.*, vol. 330, no. 24, pp. 5982–6005, Nov. 2011.

[60] S. Alkoy, A. C. Hladky, A. Dogan, J. K. Cochran, Jr., and R. E. Newnham, "Piezoelectric hollow spheres for microprobe hydrophones," *Ferroelectrics*, vol. 226, no. 1, pp. 11–25, 1999.

[61] R. E. Newnham, J. K. Cochran, and S. Alkoy, "Hollow sphere transducers," U.S. Patent 6 215 231 B1, Apr. 10, 2001.

[62] Q. Kong, S. Fan, X. Bai, Y. L. Mo, and G. Song, "A novel embeddable spherical smart aggregate for structural health monitoring: Part I. Fabrication and electrical characterization," *Smart Mater. Struct.*, vol. 26, no. 9, p. 095050, 2017.

[63] Q. Kong, S. Fan, Y. L. Mo, and G. Song, "A novel embeddable spherical smart aggregate for structural health monitoring: Part II. Numerical and experimental verifications," *Smart Mater. Struct.*, vol. 26, no. 9, p. 095051, 2017.

[64] J. Wang, Q. Kong, Z. Shi, and G. Song, "Electromechanical properties of smart aggregate: Theoretical modeling and experimental validation," *Smart Mater. Struct.*, vol. 25, no. 9, p. 095008, 2016.

[65] T. T. Zhang, S. H. Dong, and W. D. Liu, "The dynamic characteristics of 2âĂŞ2 cement-based piezoelectric composite with electrode layers," *Mater. Res. Innov.*, vol. 19, no. 9, pp. S9-181–S9-186, 2015.

[66] T. Zhang, Y. Liao, K. Zhang, and J. Chen, "Theoretical analysis of the dynamic properties of a 2-2 cement-based piezoelectric dual-layer stacked sensor under impact load," *Sensors*, vol. 17, no. 5, p. 1019, 2017.

[67] J. Wang and Z. Shi, "Dynamic characteristics of an axially polarized multilayer piezoelectric/elastic composite cylindrical transducer," *IEEE Trans. Ultrason., Ferroelect., Freq. Control*, vol. 60, no. 10, pp. 2196–2203, Oct. 2013.

[68] J. J. Wang, Z. Shi, and J. Wang, "Models for designing radially polarized multilayer piezoelectric/elastic composite cylindrical transducers," *J. Intell. Mater. Syst. Struct.*, vol. 27, no. 4, pp. 500–511, 2016.

[69] W. Chen, C. Lu, J. Yang, and J. Wang, "A circular cylindrical, radially polarized ceramic shell piezoelectric transformer," *IEEE Trans. Ultrason., Ferroelectr., Freq. Control*, vol. 56, no. 6, pp. 1238–1245, Jun. 2009.

[70] S. Lin, J. Hu, and Z. Q. Fu, "Electromechanical characteristics of piezoelectric ceramic transformers in radial vibration composed of concentric piezoelectric ceramic disk and ring," *Smart Mater. Struct.*, vol. 22, no. 4, p. 045018, 2013.

[71] J. Hu, S. Lin, X. Zhang, and Y. Wang, "Radially sandwiched composite transducers composed of the radially polarized piezoelectric ceramic circular ring and metal rings," *Acta Acust. United Acust.*, vol. 100, no. 3, pp. 418–426, 2014.

[72] Y.-D. Li, K. Y. Lee, and N. Zhang, "A generalized hypergeometric function method for axisymmetric vibration analysis of a piezoelectric actuator," *Eur. J. Mech. A-Solids*, vol. 31, no. 1, pp. 110–116, 2012.

[73] S. Lin, Z. Fu, X. Zhang, Y. Wang, and J. Hu, "Radially sandwiched cylindrical piezoelectric transducer," *Smart Mater. Struct.*, vol. 22, no. 1, p. 015005, 2013.

[74] J. O. Kim, J. G. Lee, and H. Y. Chun, "Radial vibration characteristics of spherical piezoelectric transducers," *Ultrasonics*, vol. 43, no. 7, pp. 531–537, 2005.

[75] W. Q. Chen, L. Z. Wang, and Y. Lu, "Free vibrations of functionally graded piezoceramic hollow spheres with radial polarization," *J. Sound Vib.*, vol. 251, no. 1, pp. 103–114, 2002.

[76] H. J. Ding, H. M. Wang, and W. Q. Chen, "Transient responses in a piezoelectric spherically isotropic hollow sphere for symmetric problems," *ASME J. Appl. Mech.*, vol. 70, no. 3, pp. 436–445, 2003.

[77] H. M. Wang and H. J. Ding, "Dynamic analysis of a composite hollow sphere composed of elastic and piezoelectric layers," *Arch. Appl. Mech.*, vol. 76, nos. 5–6, pp. 249–262, 2006.

[78] J. Wang, P. Wei, L. Qin, and L. Tang, "Modeling and analysis of multilayer piezoelectric-elastic spherical transducers," *J. Intell. Mater. Syst. Struct.*, vol. 29, no. 11, pp. 2437–2455, 2018, doi: 10.1177/1045389X18770868.

[79] I. S. Gradshteyn and I. M. Ryzhik, *Table of Integrals, Series, and Products*, 7th ed. New York, NY, USA: Academic, 2007.

[80] P. W. Drenkow and C. F. Long, "Radial vibration of a thick-shell hollow piezoceramic sphere," *Acta Mech.*, vol. 3, no. 1, pp. 13–21, 1967.

[81] M. Hussein and P. R. Heyliger, "Discrete layer analysis of axisymmetric vibrations of laminated piezoelectric cylinders," *J. Sound Vib.*, vol. 192, no. 5, pp. 995–1013, May 1996.

[82] D. Kim, J. O. Kim, and S. I. Jung, "Vibration characteristics of a piezoelectric open-shell transducer," *J. Sound Vib.*, vol. 331, no. 9, pp. 2038–2054, Apr. 2012.

[83] M. Hussein and P. Heyliger, "Three-dimensional vibrations of layered piezoelectric cylinders," *J. Eng. Mech.*, vol. 124, no. 11, pp. 1294–1298, 1998.

JIANJUN WANG received the Ph.D. degree from Beijing Jiaotong University, Beijing, China, in 2016. He is currently a Lecturer with the Department of Applied Mechanics, University of Science and Technology Beijing, Beijing. His research interest is piezoelectric structures and devices, and their application in engineering.

QINGZHAO KONG received the B.S. degree from Shanghai Jiao Tong University in 2010 and the Ph.D. degree from the Department of Mechanical Engineering, University of Houston, in 2015. He is currently a Research Associate with the Center For Photonics Technology, Virginia Tech. He is an expert in ultrasonic, piezoceramic-based transducers, wavelet analysis, and structural health monitoring. He has participated in related research funded from the National Science Foundation, the Department of Energy, the National Aeronautics and Space Administration, and other industrial companies.

ZHIFEI SHI received the Ph.D. degree from Harbin Engineering University in 1992. Before he joined the Beijing Jiaotong University in 1994, he was with the Harbin Institute of Technology, as a Post-Doctoral Fellow, from 1992 to 1994. His research interests include smart materials and structures (with piezoelectric actuators/sensors), earthquake engineering, structural analysis, functionally graded or laminated composites, fracture and fatigue of engineering materials, variational principles, and numerical methods.

GANGBING SONG (M'95) received the B.S. degree from Zhejiang University, China, and the M.S and Ph.D. degrees from the Department of Mechanical Engineering, Columbia University, New York, NY, USA, in 1991 and 1995, respectively. He is currently the Director of the Smart Materials and Structures Laboratory and a Professor of mechanical engineering, civil and environmental engineering, and electrical and computer engineering with the University of Houston. He has expertise in smart materials and structures, structural vibration control, piezoceramics, ultrasonic transducers, structural health monitoring, and damage detection. He is a member of the ASCE and ASME. He served as the General Chair of the Earth and Space Conference 2010, Aerospace Division, and ASCE. He was a recipient of the NSF CARRER Award in 2001. He received the prestigious Outstanding Technical Contribution Award from the Aerospace Division of ASCE, the Celebrating Excellence Award for Excellence in Education from the International Society of Automation, and the IEEE Educational Activities Board Meritorious Achievement Award in Informal Education.